Advances in Industrial and Manufacturing Engineering 12 (2026) 100181

Contents lists available at ScienceDirect

Advances in Industrial and Manufacturing Engineering

journal homepage: www.sciencedirect.com/journal/advances-in-industrial-and-manufacturing-engineering

Enhancing edge integrity of high-strength steels by high-speed blanking to achieve improved crashworthiness

Olaf Schrage [a,*], Roald Lingbeek [b], Priidu Peetsalu [c], Marlon Hahn [a], Hamed Dardaei Joghan [a], Yannis P. Korkolis [a], A. Erman Tekkaya [a]

[a] Institute of Forming Technology and Lightweight Components (IUL), TU Dortmund University, 44227, Dortmund, Germany
[b] Autoliv B.V. & Co. KG, Emmy-Noether Str. 7a, 85221, Dachau, Germany
[c] AS Norma, Laki 14, 10621, Tallinn, Estonia

ARTICLE INFO

Keywords:
High-strength steel
Edge integrity
Edge stretchability
Edge crack sensitivity
Shear cutting
Blanking
Central-hole tensile-test

ABSTRACT

The increasing use of ultra-high-strength steels (UHSS) in automotive safety components is driven by stricter crash safety requirements, vehicle weight reduction, and ecological goals in production and service. The application of UHSS requires adaptations in the manufacturing process chain, as conventional slow-speed blanking (SSB) used in mass production is challenging due to tool wear. Another aspect is crashworthiness: The interaction between material properties and blanking-induced defects—such as surface irregularities, microvoids, and microcracks—promotes crack initiation at free edges and limits edge formability. Local plastic deformation without breakage is a precondition for a stable break load of safety components, wherefore edge stretchability serves as an indicator for crashworthiness. High-speed blanking (HSB) of three steels with ultimate tensile strengths in the range of 1500 MPa—martensitic Docol 1500M, press-hardened (PH) 22MnB5, and carbon steel C60—is examined. Blanking trials are followed by central-hole tensile tests (CHTT) to assess edge stretchability. HSB produces edges with high geometric accuracy and homogeneous fracture surfaces, exhibiting roughness values comparable to wire-eroded surfaces. The shear-affected zone is confined to a narrow band of less than 2% of the sheet thickness, which is four times smaller than those observed in SSB. CHTT results show that HSB edges retain the same load-bearing capacity and edge fracture strain as wire-eroded edges, showing that edge integrity has not been compromised by HSB. In contrast, SSB triggers premature crack initiation reducing the achievable fracture strain by nearly half.

1. Introduction

Increasing demands on passenger safety and lightweighting of vehicles as an aspect of sustainable design require the use of AHSS and UHSS in automotive safety components. Mass production of those components requires a blanking process which leads to no-compromise crashworthiness. Some high-strength steels are sensitive to edge cracks evolving from cutting defects such as surface irregularities, microvoids and microcracks. Edge integrity, which is the degree of such defects, is influencing formability, fatigue resistance and the crashworthiness of the steels and components (Lara et al., 2013; Casellas et al., 2017; Parareda et al., 2020).

Global metrics such as fracture elongation, tensile strength, and forming limit curves are not sufficient to classify a material's crashworthiness (Lingbeek et al., 2020). Local formability measures such as the local fracture strain in uniaxial and plane strain notched tensile tests showed a stronger correlation with respect to the crashworthiness of materials. Frómeta et al. (2019) showed a correlation of the fracture measure for crashworthiness of different steels by quantifying the dissipated energy in a ductile fracture process. According to Casellas et al. (2017) and Frómeta et al. (2017), the hole expansion ratio (HER) can be correlated with the fracture toughness value w_e, calculated based on the essential work to fracture (EWF) method by Cotterell and Reddel (1977).

Edge stretchability is governed by both material properties and shear-cutting process parameters in strong interaction. Central-hole tensile tests of the dual-phase steel DP780 show a significantly premature crack initiation and failure of punched specimens, compared to

This article is part of a special issue entitled: Advanced Sheet Metal Forming published in Advances in Industrial and Manufacturing Engineering.

* Corresponding author.
E-mail address: olaf.schrage@iul.tu-dortmund.de (O. Schrage).

https://doi.org/10.1016/j.aime.2026.100181
Received 14 September 2025; Received in revised form 15 January 2026; Accepted 26 January 2026
Available online 30 January 2026

milled and water-jet cut ones (Wang et al., 2014). Similar findings are reported by Feistle et al. (2019) for the dual-phase (DP) steel HCT980XD, tested at different blanking clearances, resulting in a reduction of the achievable edge fracture strain of at least 23%. A decrease of the HER in ISO16630 conical punch tests of blanked edges compared to wire-eroded and milled edges is reported by Larour et al. (2021) for AHSS – dual- and complex-phase steels – as well as for micro-alloyed and mild steels. For a single-phase martensitic steel with an ultimate tensile strength (UTS) of 1106 MPa, the HER of a blanked hole is only reaching 73% of the HER achieved with the wire-eroded edge (Cho et al., 2023).

Fig. 1 shows the compromised edge integrity resulting from blanking, compared to a wire-eroded edge for low-carbon steel with an ultimate tensile strength of 840 MPa, which leads to the observed lowered edge stretchability. Significantly increased surface irregularities in the form of edge shape and roughness occur for the blanked edge compared to the wire-eroded one. An increased hardness in the shear-affected zone (SAZ) due to strain hardening, ductile damage in the form of microvoids, and microcracks at the (sub-)surface further compromise the edge integrity (Plosila et al., 2024; Khalilabad et al., 2023; Mohrbacher, 2013). The dominant mechanism —reduced remaining deformability or fracture toughness of crack propagation— and the parameters influencing the formation and propagation of edge cracks, as well as their material dependence, are still under debate.

Another important aspect of shear cutting of (ultra) high-strength steels is the heavily increased load on the tool, causing early tool failure. Testing tool steels for blanking DP steels with tensile strengths of 780, 1180 and 1470 MPa, the punch edges experienced chipping and severe plastic deformation in fewer than 100,000 strokes, which poses a risk to process stability (Beier et al., 2023). Continuous stroke tests without tool breakage, but with continuous (severe) tool wear, are possible up to 40,000 strokes for a DP steel with a UTS of 1470 MPa, (Beier et al., 2023), up to 50,000 strokes for 22MnB5 in press hardened condition with an UTS of 1500 MPa (Vogt et al., 2017) and up to 1,000,000 strokes for an Ultra-High-Strength Spring Strip with a UTS of 1824 MPa (Winter et al., 2022). Even if sudden punch failure could be avoided by the selection of the tool material, worn punch and die edges reduce the edge stretchability (Feistle et al., 2019) requiring an early tool change. By increasing the blanking clearance, tool loads could be reduced (Beier et al., 2023), however, this conflicts with a reduced edge fracture strain at larger clearances (Feistle et al., 2019).

In current mass production, laser cutting is often used as an alternative to blanking since less severe defects are introduced at the cut edge and there is no risk of sudden tool failure (Mohrbacher, 2013). Laser-cut edges exhibit a heat-affected zone, kerf angle, and surface waviness that depend on process parameters and reduce edge stretchability under non-optimal conditions (Thomas, 2013). To mitigate this, laser polishing—a local heat treatment of the cut edge—has been proposed to enhance the stretchability of AHSS (Li et al., 2024). Nevertheless, all laser-based processes result in an increasing process time, energy consumption and cost compared to mechanical shearing processes (Choi et al., 2014; Landgrebe et al., 2017).

High-speed blanking, with a process principle analogous to conventional blanking except for the much-increased punch velocity, shows a potential to replace the laser-cutting operations for ultra-high strength steel sheets (Landgrebe et al., 2017). In contrast to conventional blanking, the edges produced by high-speed blanking exhibit a smooth fracture surface, with surface roughness levels similar to those seen in fine-blanking (Landgrebe et al., 2017; Drossel et al., 2012). Geometrically, the blanked edge is S-shaped, with less than 100 µm deviation from a straight edge (Schmitz et al., 2020). The edge shows only minimal roll-over and virtually no burr (Landgrebe et al., 2017; Winter et al., 2021). High-speed blanking of a 10 mm thick component made from S500MC steel (UTS of 550 MPa) revealed that the SAZ is significantly

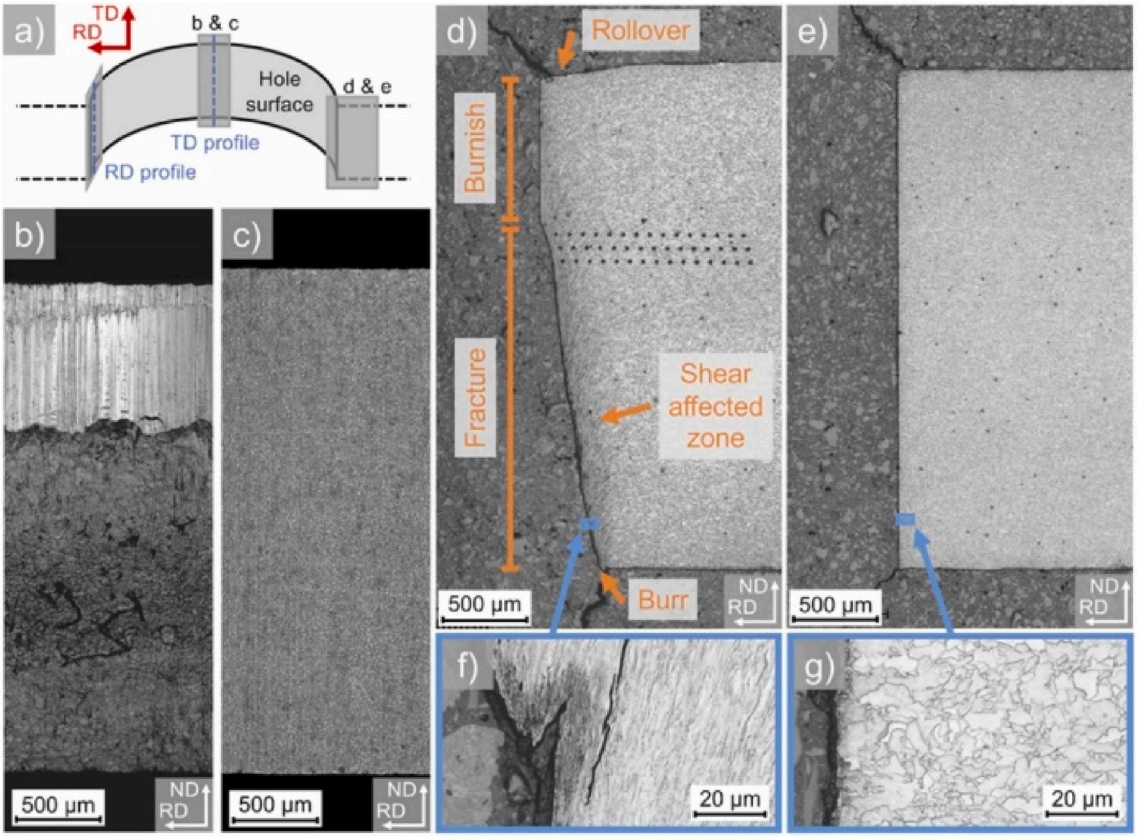

Fig. 1. Comparison of a blanked and wire-eroded edges. a) Locations of the figures; fracture surface of b) blanked and c) wire-eroded; etched cross sections of d) blanked and e) wire-eroded; and microstructure at the edges of f) blanked and g) wire-eroded specimens (Plosila et al., 2024).

smaller in HSB parts than in those created through fine-blanking (Neugebauer et al., 2011).

Considering the SAZ of the (ultra-)high-strength steels 20MnB5 (UTS of 1500 MPa) and C75S (UTS of 1380 MPa) the deformation is localized to a band of around 20–50 µm (Fig. 2), smaller than the initial blanking clearance, along an S-shaped cut edge (Schmitz et al., 2020). According to the definition provided by Dodd and Bai (2012), a shear band represents a localized region where the material transitions from uniform to concentrated strain. Building on Rogers' (1979) classification, two separate types of shear bands are evident in the high-speed blanked edge: deformation shear bands and transformation shear bands. Deformation shear bands are distinguished by intense localized plastic flow, resulting in noticeably elongated and distorted grains aligned with the direction of shear. In contrast, transformation shear bands appear as bright regions under light microscopy, signifying a structural transformation in the material. Such transformations may involve processes like grain reorientation, dynamic recrystallization, amorphization, or phase changes, including martensitic transformation or its heat-treated variants (Yan et al., 2021).

Schmitz et al. (2020) showed that the microstructure of the transformation shear band in high-speed blanking of 20MnB5 and C75S consists of nanocrystalline grains (Fig. 3b and c). The authors measured increases in hardness of 150 HV, or 30%, for 22MnB5 and 510 HV, or 95% for C75S within the transformation shear band, compared with the surrounding base material (Fig. 3a). The length and width of the transformation shear band in 22MnB5 steel depend on punch velocity and blanking clearance. Observations revealed that the transformation shear band is not forming along the entire sheet thickness, and is surrounded by the deformation shear band (Schrage et al., 2025a). The band mainly forms in the middle of the sheet, and its length extends to a maximum of two-thirds of the sheet thickness for punch velocity between 5 and 12 m/s and relative blanking clearances of 1.7–16.7% of the sheet thickness (Winter et al., 2021). This results in a hardness gradient along the sheet thickness direction and perpendicular to it. If those gradients induce similar damage mechanisms as the hardness gradient of the martensite and soft ferrite phase in DP steels, resulting in a lower edge formability, is to be determined.

Structural components (e.g. A- and B-pillars or the roof frame of a car body) are designed to retain a stable shape, hence limit their deformation, in the event of a collision to ensure passenger safety. Load-carrying components in automotive passive safety systems (e.g., seat belt buckles, buckle brackets, pillar loops or seat adjustment components) shall retain their integrity in a crash situation. Hence, these components are made from ultra-high-strength steels (commonly achieved through a heat treatment process of the stamped component). The crashworthiness of passive safety components is tested by break load tests, which are statistically evaluated to be able to rule out failures below 1 part per million, or a six-sigma level (Lingbeek et al., 2020). Besides material tensile strength, the performance of components in such a test also depends on the material's toughness, the material's resistance against crack initiation and propagation (Frómeta et al., 2019), and the stretchability

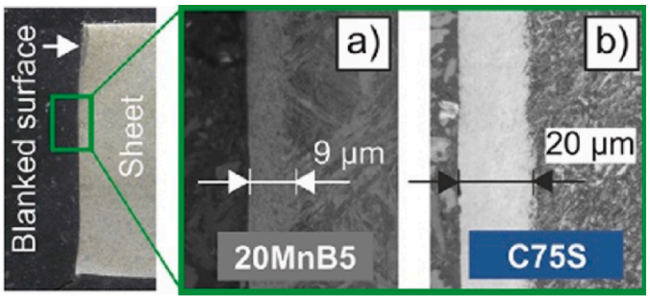

Fig. 2. Micrographs of the blanked surface of a) 20MnB5 and b) C75S (Schmitz et al., 2020).

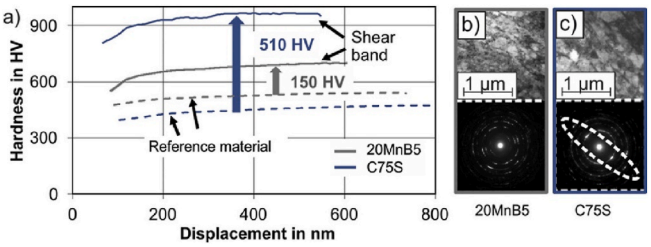

Fig. 3. Hardness increase of TSB measured by nanoindentation for C75S (blue) and 20MnB5 (grey); b) and c) TEM micrographs of the TSB in 20MnB5 and C75S (Schmitz et al., 2020).

of blanked edges (Casellas et al., 2017). In order to achieve a no-compromise level of edge quality in mass production and to overcome the limitation of blanking-induced defects as a cause for crack initiation and propagation in ultra-high-strength steels, a process chain consisting of fine-blanking with several heat treatments before and after trimming C60-carbon steel is commonly used. Soft- and spheroidisation-annealing prior to fine-blanking is applied to achieve a mild strength material with uniform distribution of spherical carbides, which is required for a tear-off and crack-free surface by fine-blanking (Zheng et al., 2019). The targeted tensile strength of 1500 MPa is achieved through hardening and annealing after trimming the components. To reduce CO2-equivalent emissions and cost, the process chain needs to be modified to process high-strength materials, with the aim of reducing the number of heat treatments required. Components made of hot-rolled Docol 1500M and trimmed by HSB would not require any heat treatment after steel manufacturing, leading to the desired ecological benefit. According to the Environmental Product Declaration of the steel supplier SSAB, the global warming potential (GWP) for the manufacture of 1 kg hot rolled steel is 1.9 kg CO_2 equivalent (SSAB, 2025b), compared to 2.17 kg CO_2 equivalent for 1 kg of cold rolled steel (SSAB, 2025a). This results in a 14% reduction in the GWP. Omitting the spheroidisation annealing, needed for fine-blanking, and omitting the hardening heat treatment of the component adds another reduction in GWP compared with the current process chain.

Consequently, High-speed blanking is tested for three ultra-high-strength steels, with prior studies existing only for one of the investigated materials: press-hardened 22MnB5. For the carbon steel C60, with its inherent microstructure, heat treatments are required to achieve a fine-blanking appropriate microstructure with a homogeneous distribution of fine carbides. High-speed blanking on the cold-rolled microstructure of C60 is investigated to potentially eliminate these heat treatments. Blanking trials are followed by central-hole tensile tests to assess edge stretchability, which serves as an indicator of crashworthiness. To isolate the effect of edge integrity on edge stretchability from the material influence, high-speed blanked edges are compared with wire-eroded reference specimens. An exemplary comparison of high-speed and slow-speed blanking highlights the significant differences in the edge characteristics and their performance in central-hole tensile tests. To date, there are no reports addressing how high-speed blanking affects the edge crack sensitivity of high-strength steels.

2. Materials and testing procedures

2.1. Materials

The three materials of this study have been selected based on the requirement for a tensile strength of approximately 1500 MPa, in order to maintain the current component design for C60-Hardened and Annealed (C60-HA) steel with an ultimate tensile strength of 1650 MPa. The first two materials are the martensitic steel Docol 1500M from SSAB and the press-hardening steel 22MnB5 from Salzgitter AG, both of which fulfil these requirements. Quasistatic tensile tests are conducted to assess

the material properties (Fig. 4). Docol 1500M, a hot-rolled martensitic steel, has an ultimate tensile strength of 1610 MPa. Due to the resulting high forming force in combination with low formability, it is suitable for components with low geometric complexity. Components with high geometric complexity can be produced using the press-hardening process and 22MnB5 steel. However, the final cut of the component must be performed on the press-hardened material. To cut the 22MnB5 steel in its martensitic state, the sheets undergo a process similar to press-hardening. This process involves austenitisation in an oven, followed by rapid cooling in a water-cooled 'forming' tool, to produce flat, hardened sheets measuring 500 × 500mm. An ultimate tensile strength of 1475 MPa is achieved for 22MnB5 press-hardened steel (22MnB5-PH). Compared to C60-HA carbon steel, martensitic steels demonstrate lower uniform elongation (a measure of global formability), but higher total elongation at fracture A_{80}. This indicates that martensitic steels exhibit better local formability, likely performing better in a CHTT, than carbon steel hardened and annealed to achieve the same material strength.

The carbon steel C60 in its delivery condition after cold rolling (C60-CR) is investigated as a third base material. If the steel is blanked in its delivery condition, without requiring soft annealing and spheroidisation, the process chain will be significantly shortened. This would be an energy-use improvement of the current process, which includes fine-blanking and requires the material to be in a soft condition with a strength below 500 MPa. Hardening the blanked component would result in the same material behavior as C60-HA. High-speed blanking of C60-HA is not considered since it is more reasonable to harden the material after blanking than before blanking.

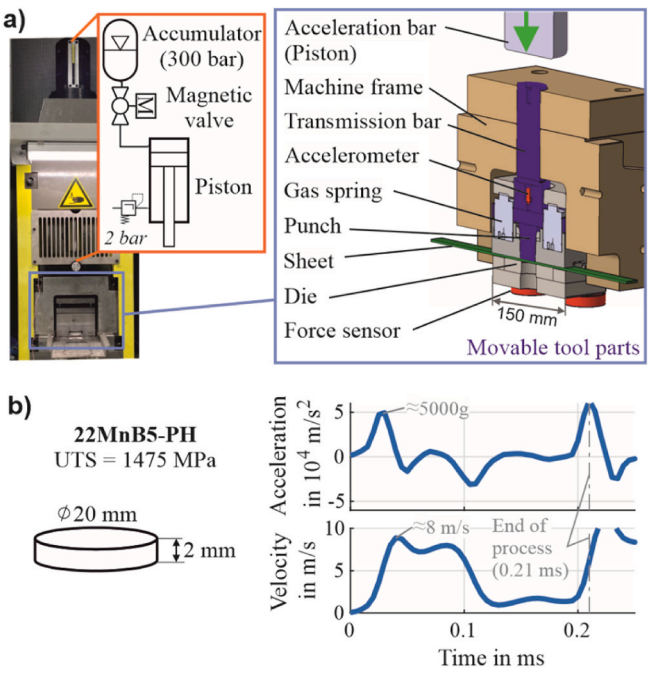

Fig. 5. High-speed blanking process principle a) machine set up of 'AdiaClip 1 kJ' b) exemplary acceleration measurements and calculated velocity profile.

2.2. Blanking experiments

2.2.1. High-speed blanking (HSB)

High-speed blanking experiments are conducted using the AdiaClip 1 kJ hydraulic impact press, which is manufactured by Adiapress, a subsidiary of MPM Emalec France (Fig. 5a). This machine generates impact energy through high-speed hydraulics and operates on a principle similar to that of a down-stroking hammer. Before each stroke, a pressure accumulator is charged to 300 bar which is then released via a magnetic valve and accelerates a double-acting hydraulic cylinder, also referred to as the "piston" or "acceleration bar". After a free acceleration over a length of 40–100 mm, depending on the machine setting, the acceleration bar hits the movable parts of the tool cassette (namely, the transmission bar) stacked on top of the punch (Fig. 5). The punch is resting directly on top of the sheet, on which a blank holder force of 24 kN is applied by gas springs. A decoupling of the tool cassette and acceleration bar is achieved as soon as the transmission bar is fully retracted into the machine housing (geometrically set to the sheet thickness). The remaining energy of the acceleration bar is absorbed by the machine frame. The initial impact energy can be continuously varied between 300 J and 1000 J by adjusting the acceleration length of the striker bar, while the bar's geometry and mass remain constant. As a result, impact energy and punch velocity cannot be controlled independently. The resulting process kinematics are measured by a piezoelectric accelerometer (PCB Series 350B01) on top of the punch and piezo-force-sensors (Kistler 9601) beneath the tool cassette (inset of Fig. 5a). Fig. 5b plots an exemplary acceleration measurement and the calculated velocity. The process time of 0.21 ms refers to the actual cutting phase. Its start is defined by the onset of tool movement, detected via the accelerometer signal, and its end is marked by the measured cutting force dropping to zero. During that time, the acceleration of the transmission bar is irregular due to impact and wave propagation phenomena associated with this setup. However, when the acceleration is integrated, the resulting velocity seems to be relatively constant, in the range of 8 m/s in the first 0.1 ms of the event.

In all experiments, a cylindrical punch with a diameter of 20 mm and

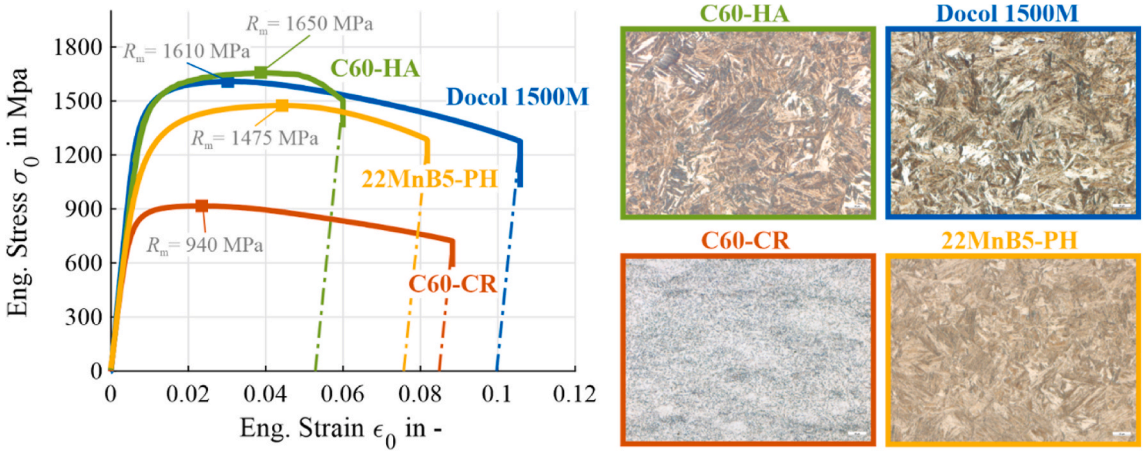

Fig. 4. Tensile test results according to DIN ISO 6892–1: A224, l_0 = 80 mm and the microstructure of the investigated materials.

an impact energy of 600 J is used. The absolute punch-die clearance c varies between 0.05 and 0.3 mm, resulting in a relative clearance c_r of between 2% and 15%, relative to the sheet thickness s of 2 mm for 22MnB5-PH and 3 mm for Docol 1500M, C60-CR, and C60-HA.

2.2.2. Slow-speed blanking (SSB)

Blanking experiments at a punch velocity of ≈ 1 mm/s, i.e., 4 orders of magnitude less than in the high-speed case, are carried out by installing the blanking tool from the high-speed impact press (Fig. 5a) to a Zwick Z250 servo-motor-driven, universal testing machine of 250 kN force capacity (Fig. 6a). Both assemblies are identical except for the press drive concept, allowing the influence of the punch velocity (Fig. 6b) to be studied in isolation. The cutting velocity in slow-speed blanking is determined by a laser displacement measurement with the sensor positioned to face the bottom of the sheet.

2.3. Analysis of blanked edge characteristics

The blanked edge surface is analyzed using microscopic images with 40× magnification and a 3D-height profile measurement obtained with a stripe light interferometer, Keyence VR5000. Based on the 3D-height profile, line measurements could be extracted to obtain the surface roughness. The SAZ at the blanked edge is analyzed by light microscopy of the metallographically prepared cross-section at the vertical centerline of the sheet (strained edge in CHTT, position marked on the slug before cutting). Water jet cutting is performed on an 'Accutom' cut-off machine from Struers using a diamond saw blade and a water-based cooling fluid. Wet abrasive sectioning at a low feed rate ensures a low cutting force and thus no deformation, as well as a plane cut with minimal heating, due to the cooling of the saw blade and specimen during the cutting process. The specimens are moulded in black bakelite hot mounting resin (180 °C) with carbon filler, polished and etched with 2% Nital.

2.4. Central-hole tensile test

To investigate the edge crack sensitivity of the blanked edges, the CHTT with a diameter of 20 mm and a sheet width of 40 mm is selected, Fig. 7. The geometry of the CHTT-specimens concentrates the strain around the lateral edges of the hole, perpendicular to the direction of applied force (Fig. 7). This concentration triggers specimen failure developing from the hole edge, allowing to analyze the influence of edge quality on the local formability. To separate the influence of local formability of different materials from the influence of blanked edge quality, wire-eroded (WE) hole edges are used as a reference. Since a wire-eroded CHTT specimen was not available for all investigated steels, machined (milled; MA) edges with a comparable edge stretchability to

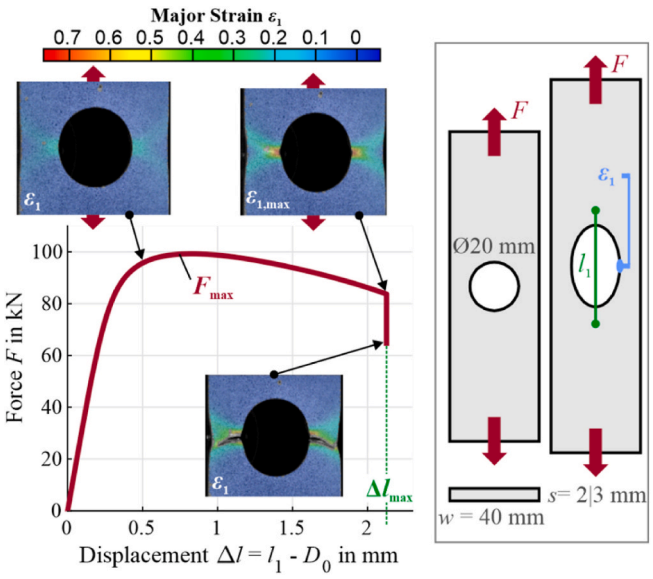

Fig. 7. Central-hole tensile test (CHTT) specification, force-displacement response and evaluation (Schrage et al., 2025c). Shown are contours of the first principal strain (true).

those of eroded edges are also included in the comparison as a reference.

The CHTTs are performed using the Zwick Z250 universal testing machine, coupled with a GOM Aramis 4M digital image correlation (DIC) system. The specimens are clamped using hydraulic specimen holders with a closing pressure of 300 bar. The DIC system consists of two CCD cameras (resolution: 2358 × 1728 pixels), each equipped with a 50 mm Titanar lens. The spatial arrangement of the cameras provides a measurement field of 65 mm by 48 mm, with a facet size of 0.39 mm (15 × 15 pixels). In line with the method described by Wang et al. (2014), displacement is determined by tracking the distance along the axis of loading between two points 2 mm apart from the upper and lower boundaries of the deformed hole, forming the basis of the force–displacement relationship. The peak load (F_{max}) measured in each test is used to assess how edge quality affects the structural load-bearing capacity. To evaluate local formability variations caused by different edge characteristics as a consequence of the manufacturing method, the major (ε_1) and minor (ε_2) strains are calculated in the vicinity of both the left and right hole edges. Due to limitations related to pattern size, camera resolution, and the facet size used in the DIC measurements, reliable and comparable strain measurements for all specimens could only be obtained with a small offset from the hole edge (Gower et al., 2005). The induced strain gradients along the circumference of the hole

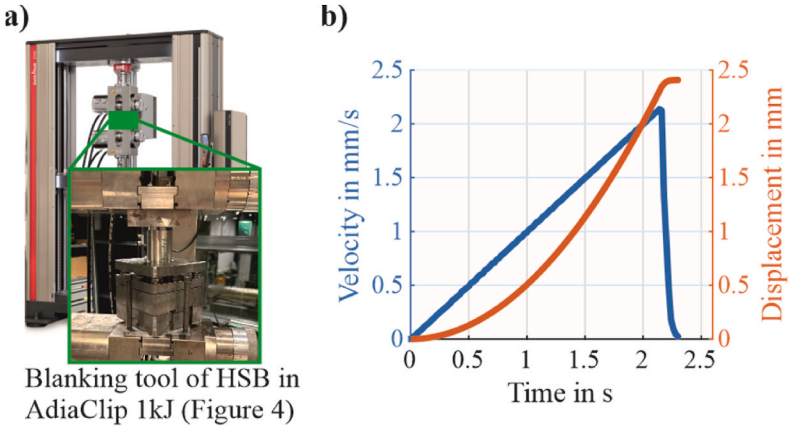

Fig. 6. Slow-speed blanking process a) set up in a universal testing machine b) exemplary velocity profile.

and perpendicular to the edge of the hole with a maximum achievable strain directly at the physical edge (Schneider et al., 2015), require a unique evaluation point of the strains to ensure comparability. The major strain-at-fracture $\varepsilon_{1,max}$ from a location situated 0.75 mm away from the hole's boundary, recorded in the final frame before fracture, is used as the characteristic strain value to rate the edge stretchability. In the tests, a measurement frequency of 1 Hz for DIC and a crosshead speed of 0.01 mm/s is used.

3. Blanked edge characteristics

As reported in Section 1, high-speed blanked edges exhibit distinctive characteristics in terms of their fracture surface and microstructure in the shear-affected zone. This section analyses the influence of the HSB process parameters applied to blanking the three steels under investigation. For 22MnB5-PH, parameter variations include the comparison of high- and slow-speed blanking as well as the variation of the relative blanking clearance in the range of 2.5% up to 15% of the sheet thickness. The investigations on Docol 1500M and C60-CR are limited to a relative blanking clearance variation of 2, 4 and 6% to modify the transformation shear bandwidth. Based on the CHTT specimen, a blanking punch with a diameter of 20 mm is used, along with dies of varying diameters, to set different clearances. In the analysis, the resulting coin is referred to as a 'slug', while the future CHTT specimen is referred to as a 'sheet'.

3.1. High-speed blanking (HSB) of 22MnB5

Fig. 8 summarizes the edge characteristics of HSB of 22MnB5-PH with a sheet thickness of 2 mm and a relative clearance c_r of *5%* with respect to the sheet thickness. The high-speed blanked edge is characterized by a nearly 100% fracture surface (Fig. 8). Only at the top of the sheet and at the bottom of the slug, a small burnish zone of less than 5% of the sheet thickness can be observed. The burnish and fracture zones are separated by a clearly visible edge in the 3D-height profile (Fig. 8c). Even if the burnish and fracture zone could clearly be separated optically, roughness measurements within both areas do not show any significant difference. Roughness measurements along the circumference of the sheet shown later (Fig. 11b) result in a mean roughness R_a of 1.4 (± 0.2) µm and an average roughness depth R_z of 8.4 (± 0.9) µm. In comparison, a wire-eroded edge has a mean roughness R_a of 2.2 (± 0.15) µm and a mean average roughness depth R_z of 17 (± 3.1) µm. A deviation of 100 µm (equivalent to the blanking clearance) from an ideal rectangular and straight edge takes the form of an S-shaped profile through the sheet thickness (Fig. 8b), as reported by Schmitz et al. (2020) and Winter et al. (2021) for 22MnB5-PH with sheet thicknesses of 4.8 mm and 3 mm. Since roll-over is almost non-existent, the corners remain rectangular. The burr is negligible at less than 10 µm in height. Both of these features are significantly reduced compared to slow-speed blanking, as will be discussed in Section 3.2. Similar observations have been reported for 22MnB5-PH by Winter et al. (2021) and Landgrebe et al. (2017).

In high-speed blanking of 22Mnb5-PH with a relative clearance of 5% and punch velocity of approximately 8 m/s, shown earlier in Fig. 5, the following shear band characteristics were identified at the blanked edge (Fig. 9): a transformation shear band emerges approximately one-third of the way through the sheet thickness, with a width that varies along the cross-section and reaching up to 20 µm. A deformation shear band is observed at two-thirds of the sheet thickness, with a maximum width of approximately 25 µm. The width of the deformation shear band (DSB), characterized by elongated grains in the shearing direction, and the TSB, characterized by its white appearance, can be clearly distinguished from the undeformed material area based on its optical appearance in the light microscopic images.

Comparing the appearance of both bands at the blanked edge of the sheet and slug, a point-symmetric pattern of deformation and transformation shear band is identified. Specifically, on the slug, a transformation shear band is located roughly two-thirds of the way through the sheet thickness, starting from the top surface and extending toward the midsection. Conversely, on the sheet, a transformation shear band is present for nearly one-third of the thickness, originating from the bottom surface. The maximum transformation shear bandwidth at the slug is almost five times greater than that at the sheet, with a similar width of deformation shear band on both sides of the cut. Consequently, the region affected by shear is confined to a narrow zone characterized by DSB and TSB bands, spanning only around 1.5 % of the total sheet thickness. It is assumed that, prior to fracture, a deformation band consisting of DSBs and TSBs next to each other exists. The TSB and DSB are distributed to the sheet and slug edge depending on the fracture evolution through this deformation band. Adding the maximum width of the SAZ to the sheet and slug results in a deformation zone width prior to fracture of less than 50 µm — half of the applied blanking clearance of 100 µm. This shows that deformation is localizing in HSB.

Significant changes in edge characteristics are achieved by varying the relative clearance from 2.5% to 15% of the sheet thickness, while keeping all other process parameters constant. The results show that the

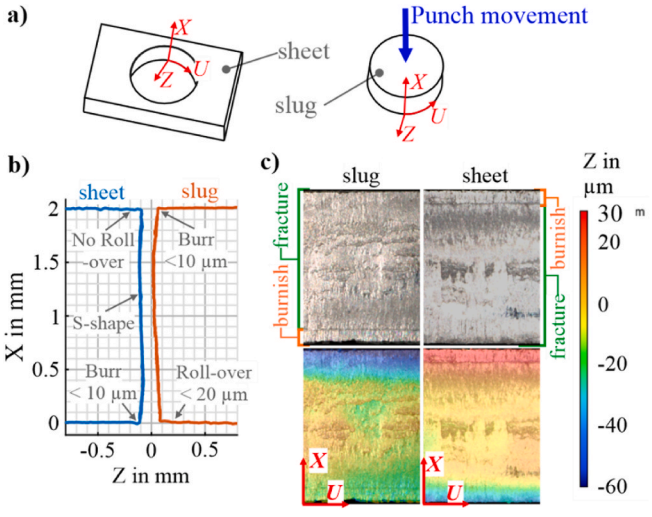

Fig. 8. Edge characteristics for 22MnB5-PH of high-speed blanking at 5% relative clearance c_r: a) Coordinate System, b) 2D-Edge profile (X-Z plane) and c) Image and 3D-height profile of fracture surface (X-U plane).

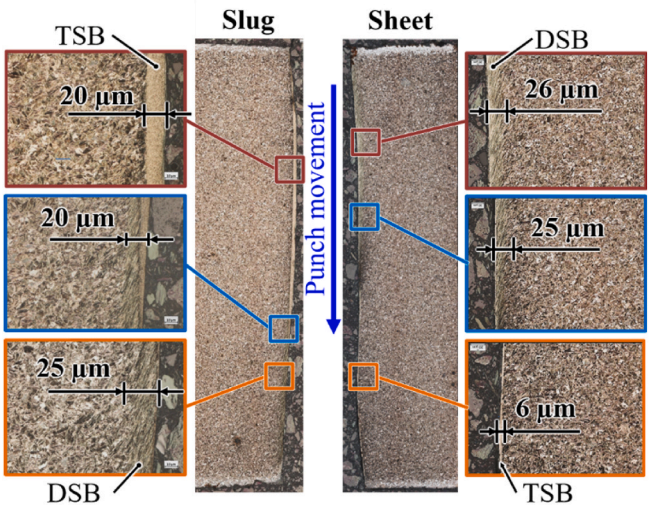

Fig. 9. Shear affected zone of sheet and slug for 22MnB5-PH of high-speed blanking at 5% relative clearance.

clearance influences the length and width of transformation shear bands, as well as the edge profile (Fig. 10). With increasing clearance, the observed S-shape deviates toward a diagonal through the clearance. For all clearances, no increase in burr size or roll-over is observed. Independent of the clearance, the SAZ is limited to a band with a maximum width of around 25 µm (<2% of the sheet thickness) along the edge shape. A TSB with a length of more than half of the sheet thickness and a maximum width of 10 µm occurs for the relative blanking clearance of 2.5%. Doubling the relative clearance to 5% of the sheet thickness, the shear bandwidth and length are almost halved. At 10 and 15% relative clearance, no transformation shear band can be observed at the blanked edge. Similar findings are reported by Winter et al. (2021) testing high-speed blanking of 3 mm thick 22MnB5-PH steel sheets with a similar hydraulic impact machine and process settings.

Independent of the clearance, the fracture surface of the blanked sheets is homogeneous and smooth, covering approximately 100% of the surface area, see Fig. 11a. Compared to a wire-eroded or machined edge, the high-speed blanked fracture surface exhibits a similar or even lower mean roughness R_a for the investigated clearances Fig. 11b.

3.2. Comparison of high-speed (HSB) and slow-speed blanking (SSB) of 22MnB5-PH

Significant differences in fracture surface characteristics and the SAZ are observed when comparing 22MnB5 blanking with 5% relative clearance at 8 m/s using an impact press (Fig. 5) and blanking four orders of magnitude slower, at 1 mm/s, using a servo-driven press (Fig. 6). While the high-speed blanked edge has a smooth fracture surface, the slow-speed blanked edge has a ragged fracture surface. In the microscopic image and 3D-height profile, the inhomogeneity of the blanked surface is clearly visible (Fig. 12). This visually apparent, non-smooth fracture surface is confirmed by roughness measurements, which show a significantly increased average roughness depth R_z (Fig. 11b). Considering the blanked edge cross-section in the metallographic images of the SSB (Fig. 13), it can be seen that surface irregularities and microcracks are present, which could potentially act as points of crack initiation and propagation. By contrast, the HSB blanked edges are smooth and show no microcracks or surface irregularities. Regarding the edge geometry, the deviation from a straight edge is below 100 µm for both high- and low-speed blanking (Figs. 8b and 12b) as a consequence

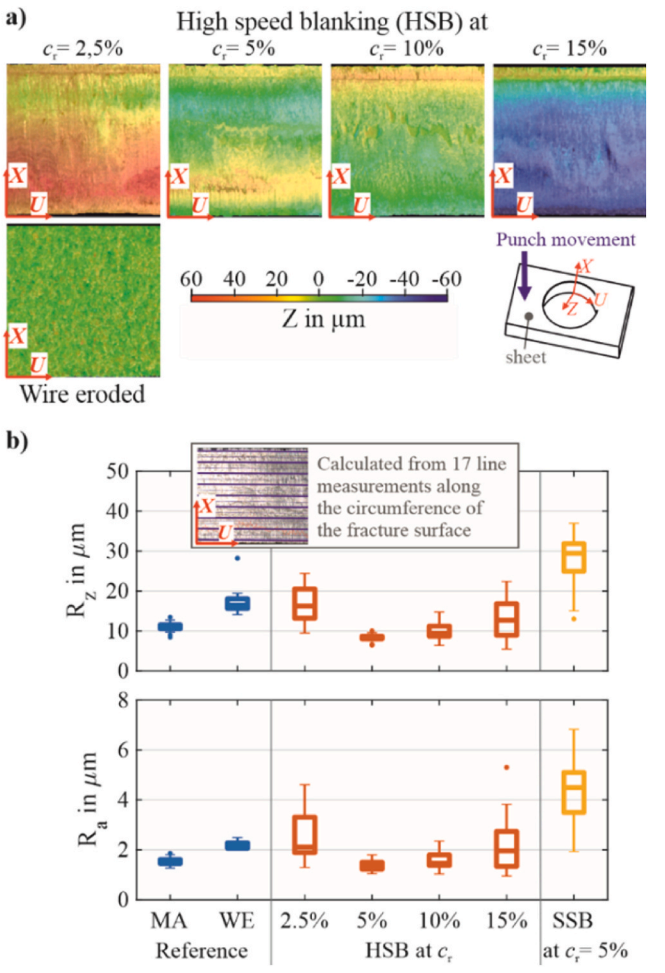

Fig. 11. Influence of the clearance on the fracture surface of the sheet for 22MnB5-PH: a) 3D-height profile and b) roughness measurements along the circumference of the blanked hole.

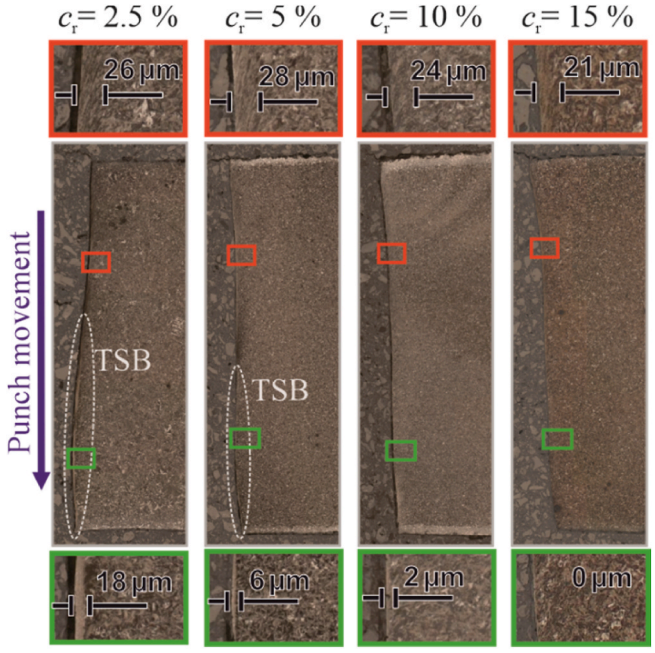

Fig. 10. Influence of the blanking clearance c in high-speed blanking on the shear affected zone for 22MnB5-PH. Shown is the sheet side.

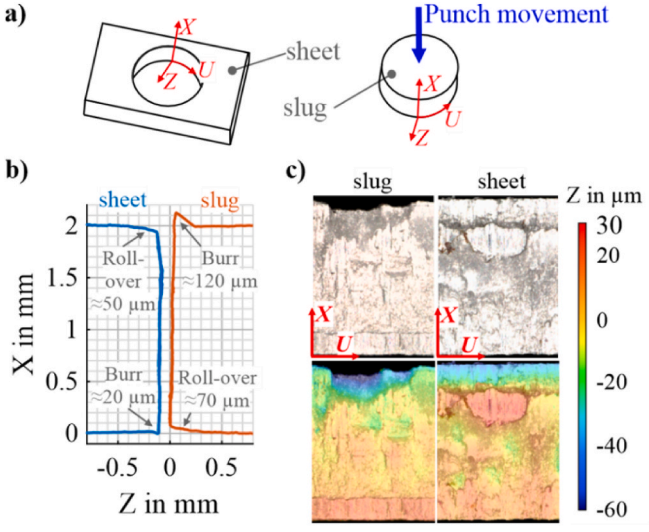

Fig. 12. Edge characteristics for 22MnB5-PH of slow-speed blanking at 5% relative clearance c_r: a) Coordinate System, b) 2D-Edge profile, and c) Image and 3D-height-profile of fracture surface.

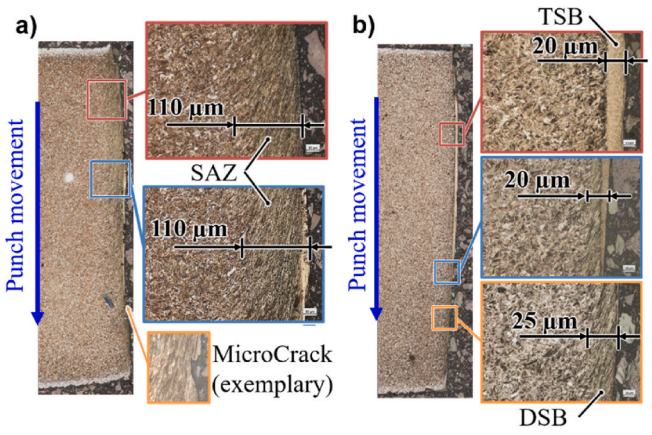

Fig. 13. Comparison of shear affected zone for a) slow- and b) high-speed blanking of 22MnB5-PH at 5% relative clearance.

of the clearance of 100 µm (c_r = 5% of sheet thickness s = 2 mm). Nevertheless, differences can be seen in the shape of the blanked edge. The SSB shows a straight burnished zone of approximately 10% of the sheet thickness that transitions into a crack with relatively straight propagation, while the HSB edge shows a pronounced S-shape. The shape of the SSB blanked edge exhibits similar straightness (equivalent to the blanking clearance) in both low- and high-speed blanking. A roll-over of 70 µm in slow-speed blanking reduces the rectangularity compared to high-speed blanked edges. Burr formation of 100 µm in SSB, as opposed to burr heights of less than 10 µm in high-speed blanking, compromises edge quality.

An analysis of the SAZ in both blanking conditions (Fig. 13) reveals that localized deformation into a thin shear band of less than 30 µm (1.5% of the sheet thickness) is characteristic of high-speed blanking. In slow-speed blanking, the SAZ extends across the entire thickness of the sheet, maintaining a uniform width of 110 µm (6% of the sheet thickness). When the SAZs of the slug and sheet are added to the shear-deformation zone, they extend by approximately 200 µm, which is twice the blanking clearance. In contrast, the deformation zone in HSB spread over approximately 50 µm, half the size of the blanking clearance.

In slow-speed blanking, fragmentation of the white-etched layer (transformation shear band) is observed in the middle of the sheet. This layer appears at the outer edge of the deformed microstructure, where the transition from shear-deformed grains to the white-etched layer occurs. In contrast, high-speed blanking reveals a clear separation between the white-etched layer, which is identified as a transformation shear band with a nanocrystalline microstructure, and the surrounding material. Further analysis of the properties of the white-etched band in slow-speed blanking, using techniques such as high-resolution Electron Backscatter Diffraction, Transmission Electron Microscopy and nano-hardness measurements, is necessary in order to detect any similarities or differences with the transformation shear band in high-speed blanking.

3.3. High-speed blanking (HSB) of Docol 1500M

For the martensitic steel Docol 1500M with 3 mm sheet thickness, high-speed blanking is conducted with relative blanking clearances of 2%, 4% and 6% Fig. 14. The aim of the clearance variation is to achieve a high degree of straightness in the edge profile (to compare it with fine blanking edge quality), which decreases with increasing clearance as demonstrated for the 22MnB5 (Fig. 10). By the variation of the clearance, the length of the transformation shear band (TSB) is affected, while the edge geometry remains comparably straight Fig. 14. Overall, the edge properties of the 3 mm-thick martensitic Docol steel are similar

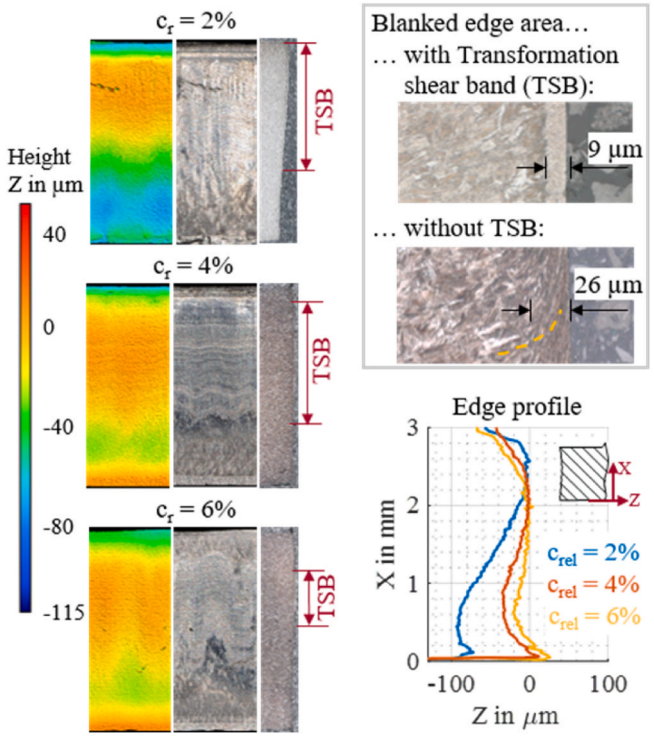

Fig. 14. Blanked edge (slug) characteristics of Docol 1500M (Schrage et al., 2025c).

to those of the 2 mm-thick martensitic 22MnB5-PH steel. Both materials exhibit a comparable microstructure and mechanical properties in quasi-static testing. The SAZ is also limited to a narrow band of approximately 1% of the sheet thickness, i.e., 20–30 µm, in both steels, independently of the sheet thickness. For Docol 1500M, the width and length of the transformation shear band increase with decreasing clearance, covering up to two-thirds of the sheet thickness. In the present investigation, no transformation shear band formed over the entire sheet thickness. The point-symmetry of the SAZ, containing DSB and TSB at the slug and sheet, is similar to the observations reported in Section 3.1 for 22mnB5-PH.

Two distinct areas with a different optical appearance of the fracture surface can be detected in the microscopic images. A shinier surface is observed at the areas where a TSB is present in the cross-section of the blanked edge. The fracture surface area, coinciding with the appearance of the deformation shear band is less shiny but has a similar surface roughness with a mean roughness R_a below 2 µm.

3.4. High-speed blanking (HSB) of C60-cold rolled (CR)

Despite the inherently non-uniform microstructure after cold rolling, high-speed blanking of C60-CR produces a smooth and homogeneous fracture surface Fig. 15. To prevent cracking and tearing at the blanked edge during fine-blanking, the distribution of globular carbides is made uniform through soft and spheroidisation annealing prior to cutting (Zheng et al., 2019). Soft annealing reduces the material strength while increasing its ductility, which is beneficial for the severe shear deformation in fine-blanking (Gram and Wagoner, 2011). Observing the microstructure in Fig. 4, C60-CR has undergone a spheroidisation annealing process prior to cold-rolling, resulting in the resolution of carbides, which are then non-uniformly distributed by the cold rolling-induced texture before HSB is applied. The strength of C60-CR is only two-thirds of that of 22MnB5-PH and Docol 1500M. Similar to the martensitic steel grades, for HSB of C60-CR, a smooth, homogeneous fracture surface is observed for 2% and 4% relative clearance, whereas

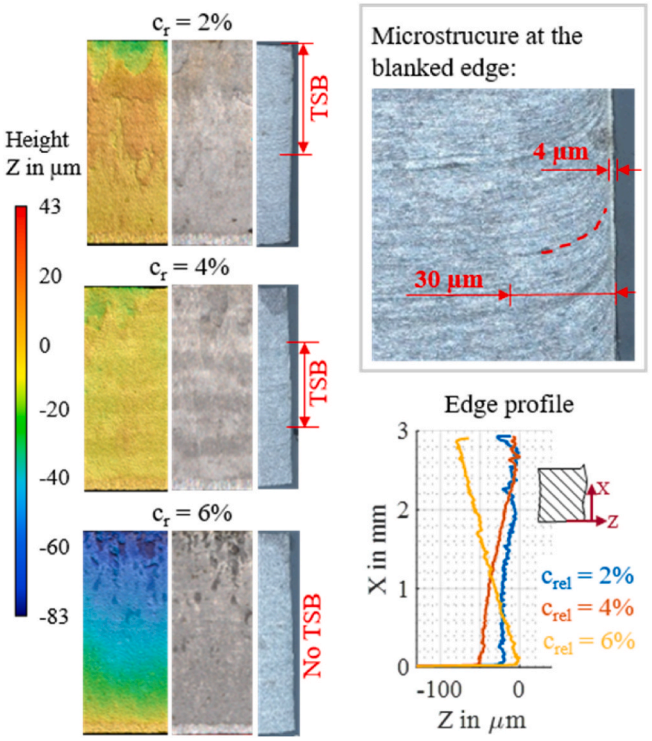

Fig. 15. Blanked edge (slug) characteristics of C60-CR (Schrage et al., 2025c).

outbreaks occur at 6% clearance Fig. 15. In contrast to the martensitic steel grades, the edge profile does not show an S-shape, as reported for HSB of high-strength steels, whereby its geometric deviation from a straight edge remains below 100 µm (less than the clearance). The SAZ along the blanked edge is characterized by a deformation shear band measuring nearly 1% of the sheet thickness, regardless of the clearance, throughout the entire thickness of the sheet. At blanked edges produced with 2% and 4% relative clearance, a thin transformation shear band with a width of less than 5 µm is observed next to the deformation shear band in the middle of the sheet. Rather than a clear separation of the two bands, a transition from deformation shear band to transformation shear band in the radial direction is observed.

Concluded from HSB investigations of other mild-strength steels, the reported edge characteristics of C60-CR are regarded as unique to HSB and not replicable by SSB, even though SSB is not performed. Blanking of the mild steels S500MC and 16MnCr5 with punch velocities ranging from 0.01 mm/s to 14 m/s showed an increase in the fracture and a decrease in the burnish area with increasing punch velocity. For punch velocities over 4 up to 14 m/s, the blanked edge is characterized by nearly 100 % fracture surface with a roughness comparable to the roughness of the burnish zone. Further, an increased straightness of the edge, judged by the angle of the fracture surface, is reported for both mild steels with increasing punch velocity (Drossel et al., 2012).

3.5. *Influence of high-speed blanking (HSB) on blanked edge features*

Based on the reported edge characteristics, it could be concluded that HSB edges are characterized by a smooth fracture surface, a SAZ less than the blanking clearance, and a good geometric accuracy characterized by a high straightness, low roll-over, and almost no burr. At small clearances, an S-shape of the edge could be observed with a deviation from a rectangular edge smaller than the blanking clearance. For the two investigated martensitic steels, 22MnB5-PH and Docol 1500M, a TSB forms with varying length and width depending on the blanking clearance. Based on previous investigations, a TSB is characterized by nanocrystalline grains and a hardness increased by 30% compared to the ground material for the martensitic steel 22MnB5-PH (Schmitz et al., 2020). The TSB on the sheet and slug appears point-symmetric, with the symmetry point in the middle of the sheet, so that the TSB is in the top half of the sheet and the bottom half of the sheet, merging into a DSB with elongated grains. Independent of TSB and DSB, its width is limited to half the clearance. In contrast, the SSB edge, blanked with equal parameters except for the punch velocity, has a SAZ of 1–1.5 times the clearance and a ragged fracture surface.

A difference of a factor of approximately 5×10^3 in punch velocity v between slow and high-speed blanking is obtained. The difference in the engineering equivalent strain rate, $\dot{\bar{\varepsilon}}$ (Equation (1)), can be estimated to first order by assuming a constant shear velocity, $\dot{\gamma}$, over the clearance, c. This results in an engineering equivalent strain rate of $\dot{\bar{\varepsilon}} = 10/\mathrm{s}$ for SSB and $\dot{\bar{\varepsilon}} = 10^5/\mathrm{s}$ for HSB, which differs by 4 orders of magnitude.

$$\dot{\varepsilon} = \frac{1}{\sqrt{3}}\dot{\gamma} \rightarrow \dot{\bar{\varepsilon}} \approx \frac{1}{\sqrt{3}}\frac{v}{c} \text{ with } \dot{\bar{\gamma}} = \frac{v}{c} \tag{1}$$

According to Schmitz (2025), the ascertained process time of 0.21 ms for steel in high-speed blanking results in quasi-adiabatic conditions during the process, as defined by a Fourier number of less than 0.01. Quasi-adiabatic means that the heat generated by plastic deformation in the deformation zone is not conducted to the surrounding material during the process. After the process, the deformation zone cools rapidly due to the temperature gradient with the undeformed material areas. On the other hand, in slow-speed blanking, with a process time of 2 s, heat conduction is possible. Numerical simulations of HSB of 22MnB5-PH show that with given process parameters, the temperature increase is significant enough to trigger thermal softening of the material in the shear region (Schrage et al., 2025b). This is leading to a deformation zone with a width smaller than the clearance and a further increase in the strain rate than calculated by the engineering strain rate (Equation (1)). This thermoplastic shear instability in blanking (Dodd, 1983) is often referred to as ‘adiabatic shear localization’ or ‘adiabatic shear failure’, since this intense localized shearing often leads to failure under dynamic loading (Dodd and Bai, 2012). The localized shear can be seen in DSB with a width smaller than the blanking clearance over which the shear strain is induced. The formation of the TSB could be explained by dynamic rotational recrystallization (DRX) mechanisms consisting of the following steps: rearrangement of dislocations into elongated dislocation cells (i.e., dynamic recovery); formation of elongated subgrains; break-up of subgrains into equiaxed micrograins; and grain rotation (Meyers et al., 2000). The formation of new grains and the rotation of grains in DRX reduce the density of dislocations, thereby lowering the macroscopic material flow stress and enhancing localization (Yan et al., 2021). Investigations on adiabatic shear localization in titanium alloys of Rittel et al. (2008) and Guo et al. (2020) indicate that DRX is triggering a softening prior to a significant temperature rise, resulting in thermal softening. Although the mechanisms of shear localization and TSB formation in HSB are still under debate, HSB leads to significantly different edge properties compared to SSB. Due to the severe plastic deformation and hardness increase at the blanked edge, the formability of the edge is to be determined (Section 4). If the SAZ in HSB, consisting of DSB and TSB, is limiting edge formability due to brittle behavior or remains ductile has not been investigated yet.

4. Central-Hole tensile test (CHTT) results

Inducing an adiabatic shear localization in HSB of UHSS martensitic steels leads to a different edge morphology compared to SSB (Section 3). To assess the integrity of the HSB edges, central hole tensile tests (CHTTs) are performed, serving as an indicator for crashworthiness (Section 1). The variation of HSB process parameters and the use of two different martensitic steels are employed to demonstrate the influence of the process and not just the favorable design of the material for preventing edge cracks. In particular, it is addressed whether a TSB

compromises the edge ductility by triggering brittle failure due to its hardness. Investigations of C60-CR provide insights into whether HSB also yields a favorable edge integrity for a non-martensitic microstructure.

4.1. Assessing material's local formability

Global formability refers to a sheet metal's ability to undergo uniform plastic deformation throughout the part without local necking. Local formability, on the other hand, refers to the material's ability to withstand plastic deformation in small, highly stressed areas—e. g. after necking or bending of tight radii—without fracturing. Local formability is a crucial factor for the application of high-strength steels in crash-related components (Hance, 2016). In addition to the material's global formability, edge formability must be considered for high-strength steels to predict material behavior under concentrated local deformation (Casellas et al., 2017). Therefore, CHTT's are performed on wire-eroded edges to assess the material's local formability without any cutting-induced effects. The material's performance of the CHTTs is compared using the maximum force in the central-hole tensile test F_{max} and the maximum displacement achieved Δl_{max}, evaluated at the last frame before fracture. Fig. 16 plots the mean force-displacement curve of the CHTTs (based on 10 repeats of each condition) for the three materials tested, compared to C60-HA used in current components. Comparing the load-bearing capacity by the technical stress σ_{lb} (Equation (2)), defined by the maximum force in CHTTs F_{max} divided by the initial surface area at the lateral hole edges A_0, allows to account for different sheet thicknesses of the tested materials.

$$\sigma_{lb} = \frac{F_{max}}{A_0} = \frac{F_{max}}{(w - d_0)s_0} \tag{2}$$

The determined load-bearing capacity σ_{lb} correlates with the tensile strength R_m of all the examined steels and can be estimated by multiplying the tensile strength by the initial loaded surface area A_0. The C60-HA steel has the highest load-bearing capacity, closely followed by Docol 1500M (6% difference of F_{max}). A pronounced post-necking behavior of Docol 1500M before specimen failure shows a higher local formability of Docol 1500M compared to C60-HA. The displacement at fracture Δl_{max} is increased by a factor of 1.6, resulting in more than double the achievable local major strain-at-fracture at the hole edge (Fig. 19), while both steels have comparable load-bearing capacities. A significant difference in the necking behavior of those steels is visible when comparing the cross-sectional area of the fractured CHTT specimens. According to Fonstein (2015), the homogeneity of the martensitic microstructure results in high local formability at high material strength despite a low global formability. Consequently, components made of the martensitic steel Docol 1500M would absorb more energy in the event of a crash than components made of C60-HA, since the former material can undergo greater plastic deformation at a comparable load.

The 22MnB5-PH steel achieves around 90% of the load-bearing capacity of Docol 1500M and C60-HA and shows enhanced local formability compared to C60-HA, though this is lower than that of Docol 1500M. A lower yield strength of 22MnB5-PH is leading to an earlier uniform plastic deformation in the CHTT compared to Docol 1500M and C60-HA. Strain hardening upon loading delays the maximum force in comparison with the displacement at maximum force for the two materials Docol 1500M and C60-HA. C60-CR steel requires hardening to reach the targeted load-bearing capacity, since in its delivered state, it is only 2/3 of the required one. Notably, the hardening and annealing treatment of C60 results in higher strength and slightly higher local formability, as a larger displacement before fracture can be achieved in the hardened-annealed state (C60-HA) than in the cold-rolled delivery conditions (C60-CR) of the steel.

4.2. Edge ductility of slow-speed blanked (SSB) and high-speed blanked (HSB) edges for 22MnB5

Fig. 17 shows the central-hole tensile test results of 22MnB5-PH for different blanking clearances in high-speed blanking in comparison to a wire-eroded reference sample and the slow-speed blanking with 5%

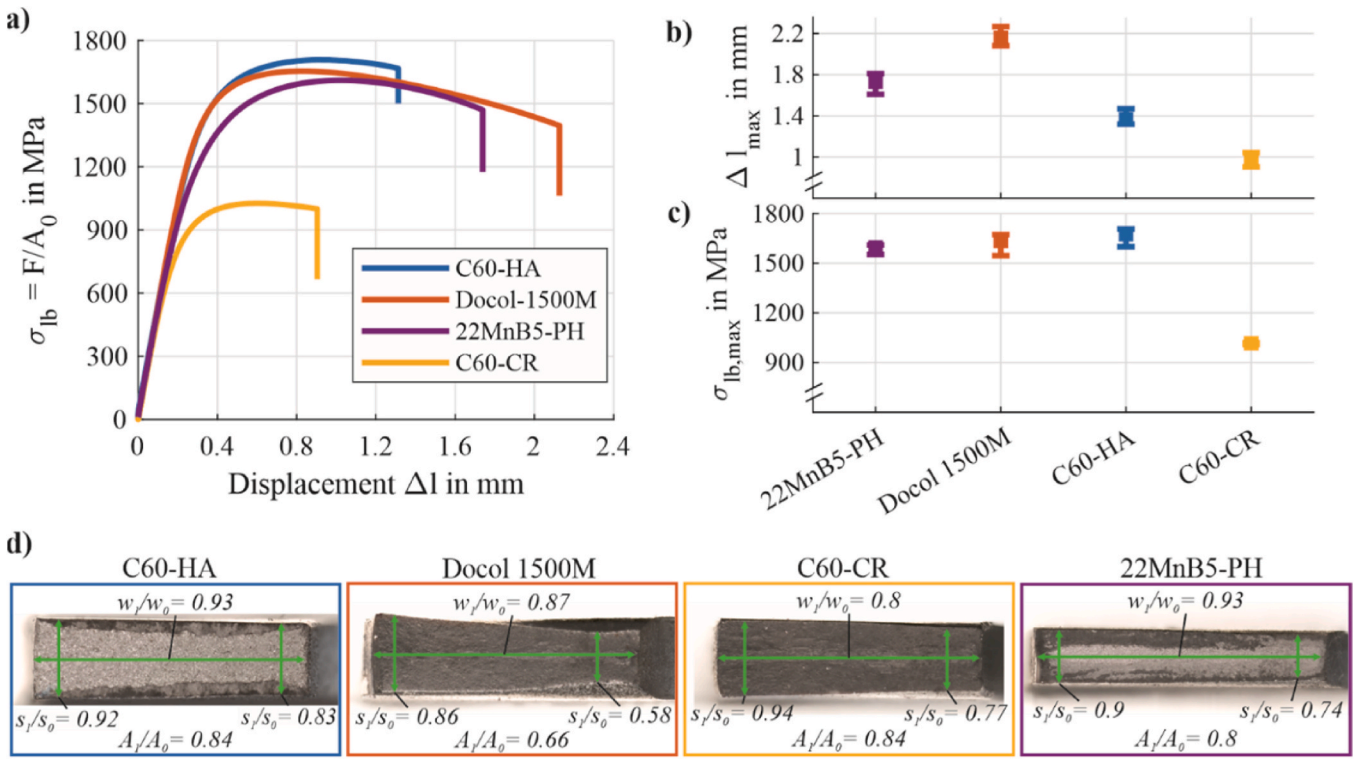

Fig. 16. Influence of material properties (wire-eroded edges) on the CHTT results: a) mean force-displacement curve of 10 repeats for each condition, b) displacement at fracture Δl_{max} and c) load-bearing capacity σ_{lb}, d) Fractured cross-section of CHTT specimen (hole on right side).

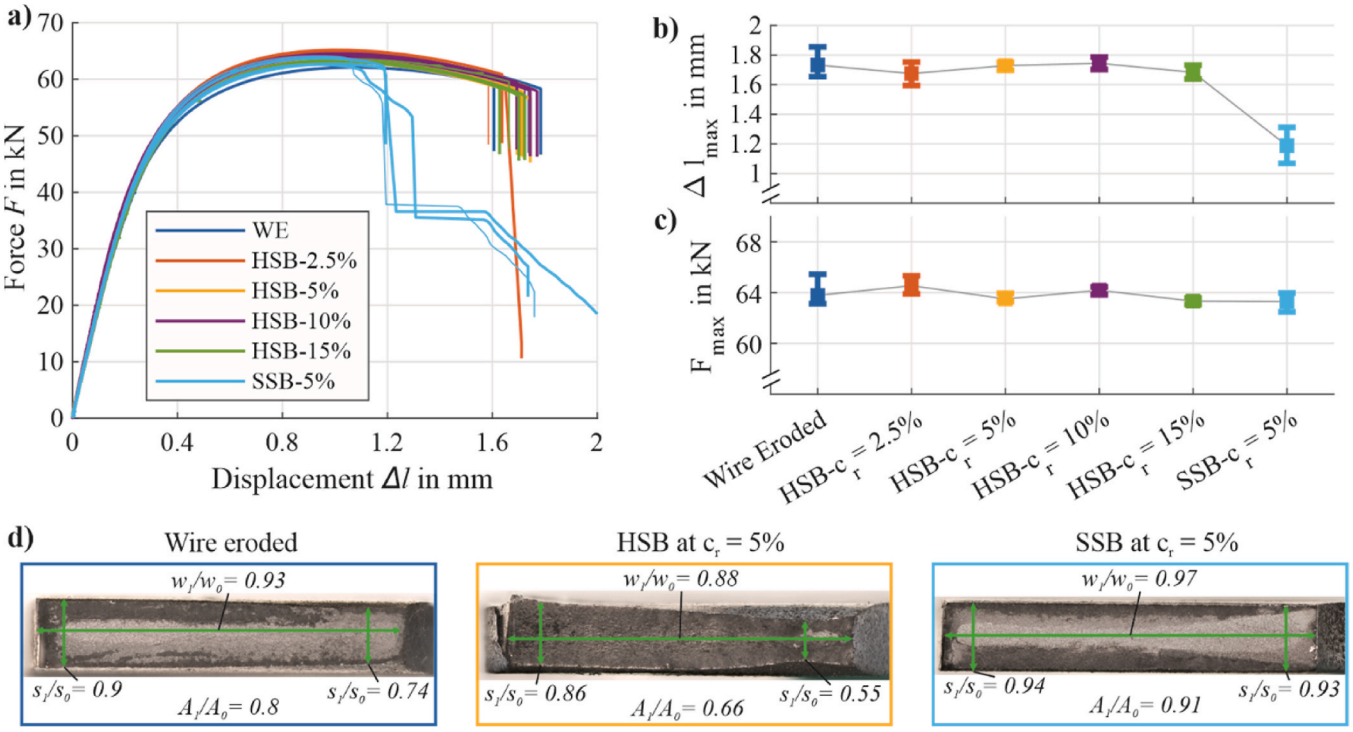

Fig. 17. Central-hole tensile test evaluation for 22MnB5 with wire-eroded (WE), high-speed blanked (HSB), slow-speed blanked (SSB) edges: a) force-displacement curves (4 repeats of each condition plotted), b) displacement at fracture Δl_{max} and c) maximum force F_{max}, d) Fractured cross-section of CHTT specimen (hole on right side).

relative blanking clearance. The high-speed blanked edge achieves the same displacement at fracture as the wire-eroded reference samples, independent of the blanking clearance and the corresponding differences in edge characteristics (Section 3.1). In contrast, blanked edges manufactured by slow-speed blanking break around the force maximum, resulting in approximately half the maximum displacement at fracture compared with wire-eroded and high-speed blanked samples.

The load-bearing capacity, evaluated by the force maximum F_{max} in the CHTT, is comparable for HSB and SSB samples. But the edge cracks at the SSB edges initiate right after the force maximum is passed, when localized deformation around the hole edge is expected. HSB samples surpass the force maximum and could be formed while necking of the specimen edge already occurred. Microscopic images of the fractured CHTT samples after testing of SSB and HSB reveal the significant differences in achievable cross-section reduction due to necking. A further difference is that the SSB samples show a crack initiation and subsequent propagation from the hole edge, giving a gradual decline of the force-displacement curve. Failure of the high-speed blanked edges occurs by a sudden break of the specimen over the entire length. This might indicate that with high-speed blanked edges the necking strain of the specimen could be reached without crack initiation from the blanked edge. In contrast, the slow blanked edges fail immediately after necking is initiated due to a reduced edge ductility by blanking induced defects.

The main differences between HSB and wire-eroded edges are their shape and the presence of a SAZ. The roughness of the HSB edge fracture surface is comparable to that of the wire-eroded surface. Independent of the clearance in HSB, the maximum difference of the edge shape from a straight, rectangular edge is limited to 150 µm (below 20 µm for the wire eroded edge), equivalent to a 2% diameter variation of the hole along the thickness direction. All materials exhibited a localization of the SAZ into bands, either deformation or transformation ones, smaller than the clearance, with a maximum width of 30 µm (1.5% of the sheet thickness). None of the differences of HSB compared to wire eroded edge characteristics seem to influence the edge stretchability while testing the HSB samples in the ‘as-cut’ condition with non-uniform edge characteristics along the sheet thickness (width and type of SAZ – deformation and transformation shear band). Specimens with a pronounced TSB (length of 2/3 of the sheet thickness) and with no TSB, dependent on the blanking clearance, show similar performances in CHTT. Therefore, it could be concluded that the TSB with a nanocrystalline microstructure and an increased hardness compared to the ground material does not compromise the edge stretchability (e.g., due to brittle crack initiation). Yet it remains unclear whether this is because the TSB is a too thin layer to have a significant effect, if the TSB exhibits a similar formability to the base material, or if the layer, despite its increased hardness, does not exhibit a brittleness sufficient to promote edge cracking. Due to the inhomogeneity of the ‘as-cut’ edge morphology, it was not possible to study the formability of the TSB in isolation. Changing the appearance of the TSB, also the geometry and the appearance of a DSB (instead of a TSB) is present, superposing the effect of the change in TSB. Independent of the HSB parameters, a smooth, homogeneous fracture surface (with slight variation in roughness but all comparable to a wire eroded edge) is observed, which is seen as the main influence parameter for the reported improved edge stretchability compared to SSB. In contrast, SSB edges exhibit rugged fracture surfaces with outbreaks and a SAZ that is four times wider compared to HSB edges. Light microscopy reveals initial cracks at the SSB edge due to the outbreaks. These initial cracks, not observed at HSB edges, could be a starting point for crack propagation during subsequent loading of these edges, resulting in a significantly reduced edge ductility. The mechanisms behind edge crack sensitivity at blanked edges in AHSS/UHSS are still under debate. Influencing factors discussed include surface roughness, blanking-induced surface cracks, hardening, and ductile damage in the form of voids or micro-cracks within the SAZ (Khalilabad et al., 2023). Different high-strength steels exhibit varying sensitivity to crack initiation and propagation (Frómeta et al., 2019), meaning the main influencing parameters for edge crack initiation and propagation can vary depending on the material. The comparison of SSB with HSB shows that the edge ductility is not compromised by HSB but by SSB, wherefore the good results could not

just be related to the material design of 22MnB5-PH. Comparing SSB and HSB edges, a smooth fracture surface with no optically detectable (by light-microscopic images with 1000× magnification) surface defects and a reduced SAZ (reduced zone affected by ductile damage) are seen as the main influencing factors for reducing the edge crack sensitivity. In addition, Schmitz et al. (2020) stated that in HSB the tensile stresses are reduced compared to SSB, which affects the stress state-dependent damage mechanisms (Brünig and Gerke, 2011). Wire eroding and machining do not cause any defects induced by blanking, such as ductile damage resulting from plastic deformation, the evolution of micro-cracks, or induced residual stresses in the SAZ. The local formability of the material in the CHTT could be accessed by those 'reference' specimens in order to study the reduction by blanking-induced imperfections. Further investigation is required to study the dominant mechanism of enhanced stretchability of HSB compared to SSB, separating edge characteristics by a post-process modification of the blanked edge, as shown in Khalilabad et al. (2023). This is because it is not possible to change any edge characteristic in isolation by varying the process parameters and subsequently testing the edge stretchability using CHTT with the inhomogeneous 'as cut' edges. Nevertheless, the 'as cut' edge is present in an application, requiring testing of its performance, including its inhomogeneity.

4.3. Edge ductility of high-speed blanking (HSB) in Docol 1500M and C60-CR

CHTT tests of the high-speed blanked edges of Docol 1500M and C60-CR (Fig. 18) produce findings similar to 22MnB5-PH. This demonstrates that the reported findings on the stretchability of the edges of HSB can be applied to other materials. HSB and subsequent CHTT testing of the three materials under investigation revealed no difference in load-bearing capacity or achievable displacement at fracture compared to wire-eroded or machined hole edges. In the case of HSB for 3 mm thick Docol 1500M and C60-CR, variations in clearances between 2 and 6% of the sheet thickness had no effect on the CHTT test performance. These clearances were chosen since they demonstrate a significant variation in TSB length (Sections 3.3 and 3.4).

4.4. Comparison of edge fracture strain

Three factors influencing the edge stretchability of high-strength steels, as rated by the maximum achievable major strain at fracture $\varepsilon_{1,max}$ in the CHTT, can be analyzed by the conducted experiments

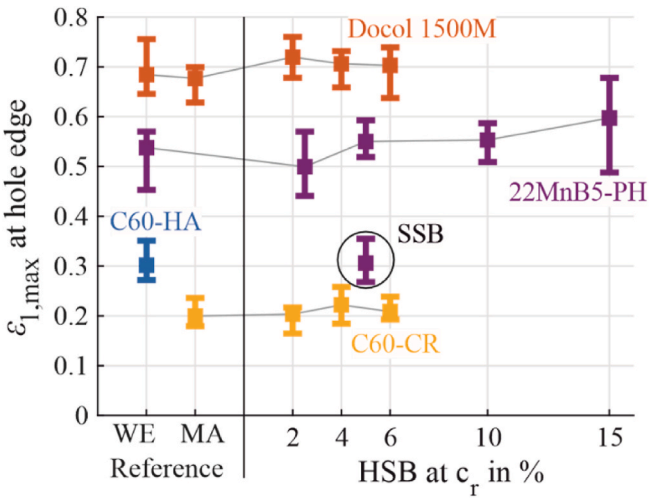

Fig. 19. Maximum major strain-at-fracture $\varepsilon_{1,max}$, at the lateral hole edge for all tested materials and edge manufacturing processes.

(Fig. 19). These factors are the material's local formability (Section 4.1), the edge integrity of HSB edges for different blanking clearances (Section 4.2 and 4.3), and the edge integrity of SSB edges (Section 4.2). Analyzing the effect of the material properties, the highest major strain at fracture $\varepsilon_{1,max}$ at the hole edge is determined for Docol 1500M. For C60-HA, the major strain at fracture is only 40% of the determined major strain at fracture in Docol 1500M with comparable material strength. The 22MnB5-PH, with 90% of the load-bearing capacity of Docol 1500M and C60-HA, reaches 80% of the major strain at fracture compared to Docol 1500M. Although all materials have a similar uniform elongation (resp. Global ductility) (Fig. 4), they exhibit different behavior in terms of local formability, resulting in different performances in the CHTT. The higher maximum achievable strain of C60-HA compared to C60-CR, along with its lower strength, underlines that local formability is not solely dependent on material strength.

HSB edge integrity does not compromise the material-specific achievable maximum strain in the CHTTs, compared to wire-eroded or machined specimens without blanking-induced imperfections. A variation of the blanking clearance and the corresponding changes in blanked edge characteristics show no influence on the attainable strain in the CHTTs. In contrast, as it is frequently reported for AHSS (cf. Section 1),

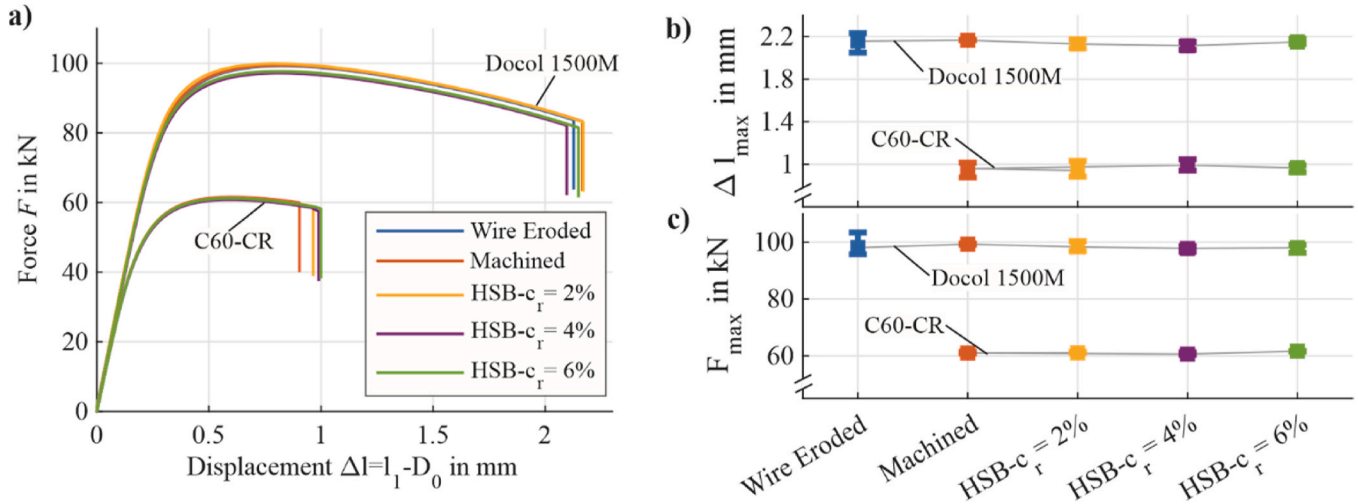

Fig. 18. Central-hole tensile test evaluation for the high-strength steels Docol 1500M and C60-HA of wire-eroded (WE) and high-speed blanked (HSB) edges at different relative clearances c_r: a) mean force-displacement curve of 10 repeats for each condition, b) displacement at fracture Δl_{max} and c) maximum force F_{max} according to (Schrage et al., 2025c).

SSB limits the major strain at fracture, since no further loading after the force maximum is possible due to edge crack initiation. The difference in edge characteristics between HSB and SSB edges leads to a major strain at fracture in the central-hole tensile test for SSB that is only half of that achieved for HSB samples under otherwise identical blanking conditions, apart from the punch velocity.

This study uses the same specimen geometry and evaluation point for the DIC measurement, enabling the influence of material properties, SSB and HSB, and HSB process parameters on each other to be assessed. To use the fracture strains determined by CHTTs for component design, the stress state and strain path of the test must be taken into account, as different edge-ductility test methods involve different stress states and strain paths, resulting in different maximum achievable edge strains (Feistle et al., 2022). For example, edge fracture strains for the same material and identical punching conditions differed in CHTTs with 10 mm and 20 mm hole diameters at a sheet width of 40 mm (Feistle et al., 2019). Kesti et al. (2022) presented an approach to incorporate the local fracture strain at an edge – dependent on the material and processing steps – by a 3D edge forming limit curve (FLC) based on multiple edge ductility tests to access different edge strain paths. If further edge ductility tests confirm that HSB does not compromise edge ductility, an 'edge FLC' to account for lower formability due to blanking-induced edge defects would not be required for component design or safety margin determination.

5. Conclusions and outlook

Driven by the motivation to change the process chain and the materials of current automotive safety components, this study investigates the HSB of three high-strength steels, the resulting edge characteristics, and edge stretchability via CHTTs. Significant differences in local formability for the three tested materials with an ultimate tensile strength of around 1500 MPa are obtained by CHTTs. The high-strength, martensitic steel Docol 1500M (UTS of 1610 MPa) achieves 2.3 times the major strain at fracture compared to the carbon steel C60-HA (UTS of 1650 MPa) and 1.3 times the major strain at fracture of the martensitic steel 22MnB5-PH (UTS of 1475 MPa). All of the steels investigated could be trimmed by HSB without compromising the maximum achievable major strain at fracture in subsequent CHTTs, compared with wire-eroded (WE) reference specimens. Although differences in edge morphology are evident, no difference in performance is observed between WE and HSB edges in the CHTT. In contrast, SSB of 22MnB5-PH results in significantly compromised formability in CHTTs, as is commonly observed with shear cutting of advanced high-strength steels (AHSS). To the authors' knowledge, no other study has reported comparable results using any variation of shear cutting.

The ability of high-speed blanking to cut (ultra-)high-strength steels without compromising edge integrity enables serving local plastic deformation without failure as a precondition for a stable break load of the components, making it a strong candidate for the manufacturing of automotive safety components. Processing hot-rolled martensitic steel using HSB in its delivery condition would eliminate the need for any heat treatment after steel production, reducing the global warming potential by over 14% compared to existing manufacturing process chains that require heat treatments to soften the material prior to fine blanking and harden it afterwards. Although CHTT results are expected to correlate with component performance in a break-load test, they cannot replicate the exact conditions of a crash incident. As a next step, it is considered to manufacture functional components using HSB and test them in various crash tests. In this context, the difference in material strength and local formability from C60-HA to Docol 1500M is also to be investigated with respect to the ‘distance to failure’ of the component. When considering changing the material and process chain, the suitability of HSB for mass production must be investigated through endurance tests of tool lifetime. Due to different material separation mechanisms arising from the quasi-adiabatic effect, the characteristics of blanked edges differ significantly between SSB and HSB. Consequently, the tool wear mechanism may also differ due to different local conditions (e.g., elevated temperature), a smooth fracture surface in combination with high geometric straightness (reducing friction and retraction forces), and low punch indentation until fracture (affecting flank wear and retraction force). The transferability of results obtained for single-phase high-strength steels to dual-phase (DP) and complex-phase (CP) AHSS remains to be investigated.

CRediT authorship contribution statement

Olaf Schrage: Writing – original draft, Methodology, Investigation. **Roald Lingbeek:** Writing – review & editing, Methodology, Funding acquisition, Conceptualization. **Priidu Peetsalu:** Validation, Resources, Methodology. **Marlon Hahn:** Writing – review & editing, Supervision, Methodology, Conceptualization. **Hamed Dardaei Joghan:** Writing – review & editing, Supervision. **Yannis P. Korkolis:** Writing – review & editing, Supervision. **A. Erman Tekkaya:** Writing – review & editing, Supervision, Funding acquisition, Conceptualization.

Declaration of competing interest

The authors declare that they have no known competing financial interests or personal relationships that could have appeared to influence the work reported in this paper.

The author is an Editorial Board Member/Editor-in-Chief/Associate Editor/Guest Editor for this journal and was not involved in the editorial review or the decision to publish this article.

Acknowledgments

The authors kindly thank German Research Foundation (DFG) and Autoliv B.V. & Co. KG for the financial support of the study, as part of the subproject TP5 of the research group FOR 5380: ‘Functional surfaces through adiabatic high-speed processes: Microstructure, mechanisms and model development - FUNDAM^{3}ENT’ (Project number 460484491 – FOR 5380).

Data availability

The authors are unable or have chosen not to specify which data has been used.

References

Beier, T., Iizuka, E., Shimmiya, T., Miyake, H., 2023. Investigation of tool damage in shear cutting of ultra-high strength sheet steels. IOP Conf. Ser. Mater. Sci. Eng. 1284, 12080. https://doi.org/10.1088/1757-899X/1284/1/012080.

Brünig, M., Gerke, S., 2011. Simulation of damage evolution in ductile metals undergoing dynamic loading conditions. Int. J. Plast. 27, 1598–1617. https://doi.org/10.1016/j.ijplas.2011.02.003.

Casellas, D., Lara, A., Frómeta, D., Gutiérrez, D., Molas, S., Pérez, L., Rehrl, J., Suppan, C., 2017. Fracture toughness to understand stretch-flangeability and edge cracking resistance in AHSS. Metall. Mater. Trans. A 48, 86–94. https://doi.org/10.1007/s11661-016-3815-x.

Cho, W., Jeong, B.-S., Jeong, K., Lee, S.-H., Kim, H., Lee, J., Kim, S.-II., Han, H.N., 2023. New approach to hole-expansion ratio in complex phase and martensitic steels: understanding the role of punching damage. J. Mater. Res. Technol. 26, 837–849. https://doi.org/10.1016/j.jmrt.2023.07.253.

Choi, H.-S., Kim, B.-M., Kim, D.-H., Ko, D.-C., 2014. Application of mechanical trimming to hot stamped 22MnB5 parts for energy saving. Int. J. Precis. Eng. Manuf. 15, 1087–1093. https://doi.org/10.1007/s12541-014-0441-7.

Cotterell, B., Reddel, J.K., 1977. The essential work of plane stress ductile fracture. Int. J. Fract. 13, 267–277. https://doi.org/10.1007/BF00040143.

Dodd, B., 1983. Shear instabilities in blanking and related processes. Met. Technol. 10, 57–60. https://doi.org/10.1179/030716983803291550.

Dodd, B., Bai, Y., 2012. Adiabatic Shear Localization. Elsevier.

Drossel, Barthel, T., Volk, W., Kopp, T., 2012. EFB-Forschungsbericht Nr. 356. Entwicklung Kalkulatorischer Kenngrößen Zur Gestaltung Von Scherschneidprozessen Und Bewertung Der Bauteilqualität Bei Anwendung Hoher Schneidgeschwindigkeiten.

Feistle, M., Golle, R., Volk, W., 2022. Edge crack test methods for AHSS steel grades: a review and comparisons. J. Mater. Process. Technol. 302, 117488. https://doi.org/10.1016/j.jmatprotec.2021.117488.

Feistle, M., Pätzold, I., Golle, R., Volk, W., 2019. Open hole tensile tests for the determination of the edge-crack sensitivity of sheared holes dependent on specimen geometry, cutting parameters, and the notch factor. Procedia Manuf. 29, 412–419. https://doi.org/10.1016/j.promfg.2019.02.156.

Fonstein, N., 2015. Advanced High Strength Sheet Steels. Springer International Publishing, Cham.

Frómeta, D., Lara, A., Molas, S., Casellas, D., Rehrl, J., Suppan, C., Larour, P., Calvo, J., 2019. On the correlation between fracture toughness and crash resistance of advanced high strength steels. Eng. Fract. Mech. 205, 319–332. https://doi.org/10.1016/j.engfracmech.2018.10.005.

Frómeta, D., Tedesco, M., Calvo, J., Lara, A., Molas, S., Casellas, D., 2017. Assessing edge cracking resistance in AHSS automotive parts by the Essential work of fracture methodology. J. Phys., Conf. Ser. 896, 12102. https://doi.org/10.1088/1742-6596/896/1/012102.

Gower, M.R.L., Shaw, R.M., Klimaytys, G.M., 2005. Development of an integrated multi-axis loading and strain mapping facility. Measurement Note.

Gram, M.D., Wagoner, R.H., 2011. Fineblanking of high strength steels: control of material properties for tool life. J. Mater. Process. Technol. 211, 717–728. https://doi.org/10.1016/j.jmatprotec.2010.12.005.

Guo, Y., Ruan, Q., Zhu, S., Wei, Q., Lu, J., Hu, B., Wu, X., Li, Y., 2020. Dynamic failure of titanium: temperature rise and adiabatic shear band formation. J. Mech. Phys. Solid. 135, 103811. https://doi.org/10.1016/j.jmps.2019.103811.

Hance, B., 2016. Advanced high strength steel: deciphering local and global formability. In: Proc. International Automotive Body Congress (IABC). Dearborn, Michigan, USA.

Kesti, V., Folmerz, M., Vierelä, R., Rautio, P., Ruoppa, R., Plosila, P., Kaijalainen, A., 2022. An approach to describe edge ductility. IOP Conf. Ser. Mater. Sci. Eng. 1238, 12035. https://doi.org/10.1088/1757-899X/1238/1/012035.

Khalilabad, M.M., Perdahcıoğlu, S., Atzema, E., van Boogaard, T. den, 2023. Initiation and growth of edge cracks after shear cutting of dual-phase steel. Int. J. Adv. Manuf. Technol. 127, 2327–2341. https://doi.org/10.1007/s00170-023-11482-2.

Landgrebe, D., Barthel, T., Schieck, F., 2017. Trimming of flat and tubular components by High speed impact cutting (HSIC). In: ASME International Mechanical Engineering Congress and Exposition. IMECE, Tampa, Florida, USA. https://doi.org/10.1115/IMECE2017-71362.

Lara, A., Picas, I., Casellas, D., 2013. Effect of the cutting process on the fatigue behaviour of press hardened and high strength dual phase steels. J. Mater. Process. Technol. 213, 1908–1919. https://doi.org/10.1016/j.jmatprotec.2013.05.003.

Larour, P., Freudenthaler, J., Pauli, H., Kerschbaum, M., Wagner, L., Felbinger, A., Sonnleitner, F., Angeli, J., 2021. Local formability assessment of AHSS steels with shear cut tensile tests. IOP Conf. Ser. Mater. Sci. Eng. 1157, 12054. https://doi.org/10.1088/1757-899X/1157/1/012054.

Li, D., Linnenbrink, S., Tekkaya, B., Dölz, M., Willenborg, E., Könemann, M., Münstermann, S., 2024. Optimizing sheet metal edge quality with laser-polishing: surface characterization and performance evaluation. Int. J. Material Form. 17. https://doi.org/10.1007/s12289-024-01847-7.

Lingbeek, R., Aldemir, B., Soni, A., Jagalur, S., Yao, L., 2020. Material spread and local failure in breakage modeling for steel safety components. Procedia Manuf. 47, 1449–1455. https://doi.org/10.1016/j.promfg.2020.04.316.

Meyers, M.A., Nesterenko, V.F., LaSalvia, J.C., Xu, Y.B., Xue, Q., 2000. Observation and modeling of dynamic recrystallization in high-strain, high-strain rate deformation of metals. J. Phys. IV France 10. https://doi.org/10.1051/jp4:2000909 pp. Pr9-51-Pr9-56.

Mohrbacher, H., 2013. Reverse metallurgical engineering towards sustainable manufacturing of vehicles using Nb and Mo alloyed high performance steels. Adv. Manuf. 1, 28–41. https://doi.org/10.1007/s40436-013-0002-9.

Neugebauer, R., Bouzakis, K.-D., Denkena, B., Klocke, F., Sterzing, A., Tekkaya, A.E., Wertheim, R., 2011. Velocity effects in metal forming and machining processes. CIRP Ann. 60, 627–650. https://doi.org/10.1016/j.cirp.2011.05.001.

Parareda, S., Casellas, D., Frómeta, D., Martínez, M., Lara, A., Barrero, A., Pujante, J., 2020. Fatigue resistance of press hardened 22MnB5 steels. Int. J. Fatig. 130, 105262. https://doi.org/10.1016/j.ijfatigue.2019.105262.

Plosila, P., Kesti, V., Hannula, J., Kömi, J., Kaijalainen, A., 2024. A comparison between tensile and hole expansion properties in 800 MPa tensile strength grade hot-rolled steels. Mater. Today Commun. 40, 109521. https://doi.org/10.1016/j.mtcomm.2024.109521.

Rittel, D., Landau, P., Venkert, A., 2008. Dynamic recrystallization as a potential cause for adiabatic shear failure. Phys. Rev. Lett. 101, 165501. https://doi.org/10.1103/PhysRevLett.101.165501.

Schmitz, F., 2025. Prozessanalyse Des Hochgeschwindigkeitsscherschneidens. Technical University Dortmund, Dissertation.

Schmitz, F., Winter, S., Clausmeyer, T., Wagner, M.F.-X., Tekkaya, A., 2020. Adiabatic blanking of advanced high-strength steels. CIRP Ann. 69, 269–272. https://doi.org/10.1016/j.cirp.2020.03.007.

Schneider, M., Geffert, A., Peshekhodov, I., Bouguecha, A., Behrens, B.-A., 2015. Overview and comparison of various test methods to determine formability of a sheet metal cut-edge and approaches to the test results application in forming analysis. Mater. Werkst. 46, 1196–1217. https://doi.org/10.1002/mawe.201500446.

Schrage, O., Dardaei Joghan, H., Hahn, M., Tekkaya, A.E., Korkolis, Y.P., 2025a. Analysis of shear localization in high-speed blanking of press-hardened 22MnB5. In: 10th International Conference on High Speed Forming – 2025. in Press.

Schrage, O., Hahn, M., Dardaei Joghan, H., Tekkaya, A.E., Korkolis, Y.P., 2025b. High-speed blanking of high-strength steel: process insights through simulation. J. Phys., Conf. Ser. 3104, 12094. https://doi.org/10.1088/1742-6596/3104/1/012094.

Schrage, O., Lingbeek, R., Peetsalu, P., Hahn, M., Joghan, H.D., Korkolis, Y.P., Tekkaya, A.E., 2025c. High-speed blanking and its potential for producing ultra-high-strength automotive safety components. MATEC Web Conf. 408, 1084. https://doi.org/10.1051/matecconf/202540801084.

SSAB, 2025a. Cold rolled coils. Environmental Product Declaration.

SSAB, 2025b. Hot rolled steel coils. Environmental Product Declaration.

Thomas, D.J., 2013. The effect of laser cutting parameters on the formability of complex phase steel. Int. J. Adv. Manuf. Technol. 64, 1297–1311. https://doi.org/10.1007/s00170-012-4087-2.

Vogt, S., Neumayer, F.F., Serkyov, I., Jesner, G., Kelsch, R., Geile, M., Sommer, A., Golle, R., Volk, W., 2017. Experimental evaluation of tool wear throughout a continuous stroke blanking process of quenched 22MnB5 ultra-high-strength steel. J. Phys., Conf. Ser. 896, 12057. https://doi.org/10.1088/1742-6596/896/1/012057.

Wang, K., Luo, M., Wierzbicki, T., 2014. Experiments and modeling of edge fracture for an AHSS sheet. Int. J. Fract. 187, 245–268. https://doi.org/10.1007/s10704-014-9937-5.

Winter, S., Nestler, M., Galiev, E., Hartmann, F., Psyk, V., Kräusel, V., Dix, M., 2021. Adiabatic blanking: influence of clearance, impact energy, and velocity on the blanked surface. JMMP 5, 35. https://doi.org/10.3390/jmmp5020035.

Winter, S., Richter, K., Galiev, E., Nestler, M., Psyk, V., Kräusel, V., 2022. Punching of ultra-high-strength spring strips: evolution of cutting edge radius up to 1,000,000 strokes for three punch materials. JMMP 6, 38. https://doi.org/10.3390/jmmp6020038.

Yan, N., Li, Z., Xu, Y., Meyers, M.A., 2021. Shear localization in metallic materials at high strain rates. Prog. Mater. Sci. 119, 100755. https://doi.org/10.1016/j.pmatsci.2020.100755.

Zheng, Q., Zhuang, X., Zhao, Z., 2019. State-of-the-art and future challenge in fine-blanking technology. Prod. Eng. Res. Dev. 13, 61–70. https://doi.org/10.1007/s11740-018-0839-7.